Article

Liquid-induced topological transformations of cellular microstructures

 Check for updates

Shucong Li[1,3], Bolei Deng[2,3], Alison Grinthal[2], Alyssha Schneider-Yamamura[2], Jinliang Kang[2], Reese S. Martens[2], Cathy T. Zhang[2], Jian Li[2], Siqin Yu[2], Katia Bertoldi[2] & Joanna Aizenberg[1,2✉]
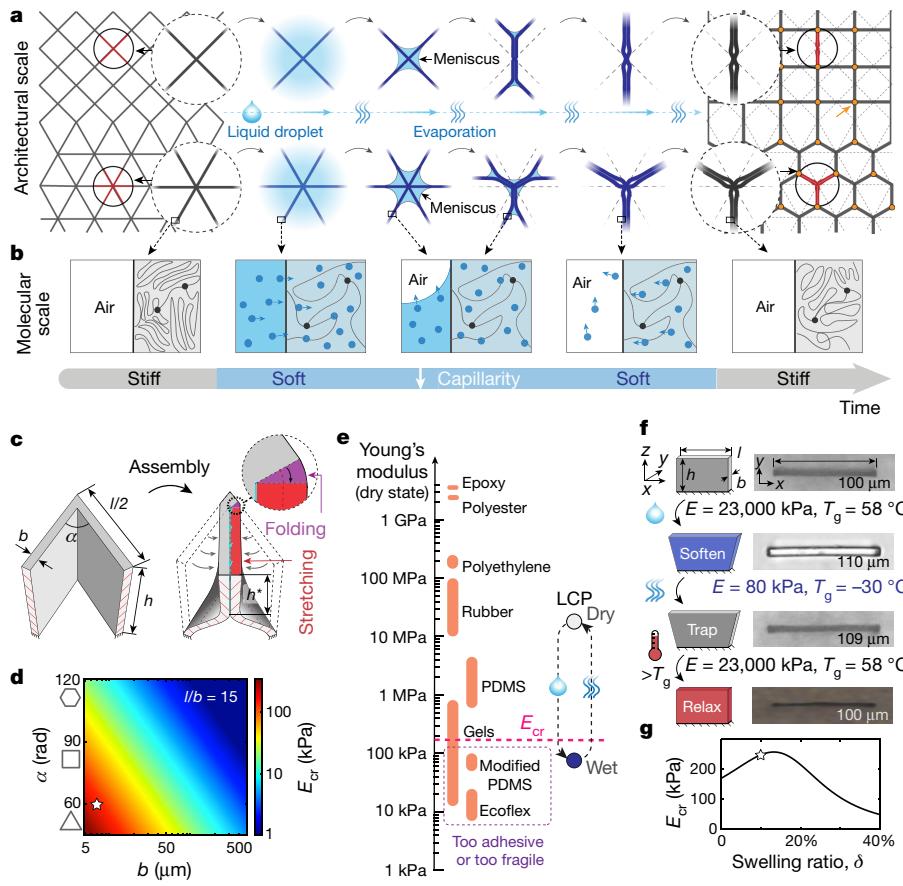
The fundamental topology of cellular structures—the location, number and connectivity of nodes and compartments—can profoundly affect their acoustic[1–4], electrical[5], chemical[6,7], mechanical[8–10] and optical[11] properties, as well as heat[1,12], fluid[13,14] and particle transport[15]. Approaches that harness swelling[16–18], electromagnetic actuation[19,20] and mechanical instabilities[21–23] in cellular materials have enabled a variety of interesting wall deformations and compartment shape alterations, but the resulting structures generally preserve the defining connectivity features of the initial topology. Achieving topological transformation presents a distinct challenge for existing strategies: it requires complex reorganization, repacking, and coordinated bending, stretching and folding, particularly around each node, where elastic resistance is highest owing to connectivity. Here we introduce a two-tiered dynamic strategy that achieves systematic reversible transformations of the fundamental topology of cellular microstructures, which can be applied to a wide range of materials and geometries. Our approach requires only exposing the structure to a selected liquid that is able to first infiltrate and plasticize the material at the molecular scale, and then, upon evaporation, form a network of localized capillary forces at the architectural scale that 'zip' the edges of the softened lattice into a new topological structure, which subsequently restiffens and remains kinetically trapped. Reversibility is induced by applying a mixture of liquids that act separately at the molecular and architectural scales (thus offering modular temporal control over the softening–evaporation–stiffening sequence) to restore the original topology or provide access to intermediate modes. Guided by a generalized theoretical model that connects cellular geometries, material stiffness and capillary forces, we demonstrate programmed reversible topological transformations of various lattice geometries and responsive materials that undergo fast global or localized deformations. We then harness dynamic topologies to develop active surfaces with information encryption, selective particle trapping and bubble release, as well as tunable mechanical, chemical and acoustic properties.

Evaporating liquids have been shown to deform and assemble simple, isolated microscale structures, such as arrays of base-attached pillars and plates, via the capillary forces of the formed liquid–vapour menisci[24–27]. We anticipated that when a liquid is applied to a cellular structure, the formation of a complex network of menisci on the interconnected geometry generates an intricate localized force field centred at each node, providing a finer level of control than can be achieved with global force fields[19,20]. However, as a base-attached interconnected structure, a cellular lattice generally requires much higher energy to deform compared to that needed for simple bending in the isolated structures, usually making capillary forces too weak for such transitions. Although the capillarity-induced reconfiguration could potentially be enabled by using a floppy material with low elastic restoring

energy[28] and high surface adhesion[26,29,30] to maintain the assembly, such systems are impractical for most applications. This apparent paradox can be resolved by introducing a transient softening of structures. It has been shown that certain liquids are able to infiltrate and soften polymeric materials at the molecular scale, thus altering their bulk mechanical properties[31–36].

On the basis of the latter considerations, we introduce a strategy to achieve fast, reversible and tunable topological transformation of cellular microstructures through capillary assembly that is broadly applicable to a wide range of geometries and materials. The key concept is that the applied liquid must not only form menisci at the architectural (micro)scale, as generally occurs in evaporation-induced assembly[24–27] (Fig. 1a), but must first transiently infiltrate, swell and plasticize the

Fig. 1 | Strategy for topological transformation of cellular structures. a, b, Schematic illustration of topological transformation occurring at the architectural scale during liquid immersion and evaporation (**a**), and corresponding changes in the polymer network at the molecular scale (**b**). Because the liquid in the compartments evaporates before the liquid inside the polymer network, the capillary forces introduced at the air–liquid interface always act on the softened structure, enabling the structure to deform and the edges to be zipped together. This results in the formation of new nodes (shown in orange and indicated by the orange arrow on the right) and the disappearance or change in connectivity of the original nodes (shown in red). **c**, Schematics of the assembly of two adjacent walls from a cellular structure characterized by angle α, edge length l, thickness b and height h. The walls are stretched and folded by the capillary forces. **d**, Contour plot of critical Young's modulus E_{cr} with respect to structural parameters α and b, with the slenderness ratio fixed at $l/b = 15$. The star marker denotes the corresponding parameters of the considered structure. **e**, List of frequently used polymeric materials and their Young's moduli in a dry state. The Young's modulus of a dry LCP changes reversibly from 23,000 kPa to 80 kPa when plasticized. **f**, Micrographs of an LCP microplate with dimensions $l = 100\,\mu m$, $b = 7\,\mu m$ and $h = 70\,\mu m$ after exposure to acetone. **g**, Critical modulus E_{cr} as a function of swelling ratio, δ. The star marker shows the swelling ratio of the selected material.
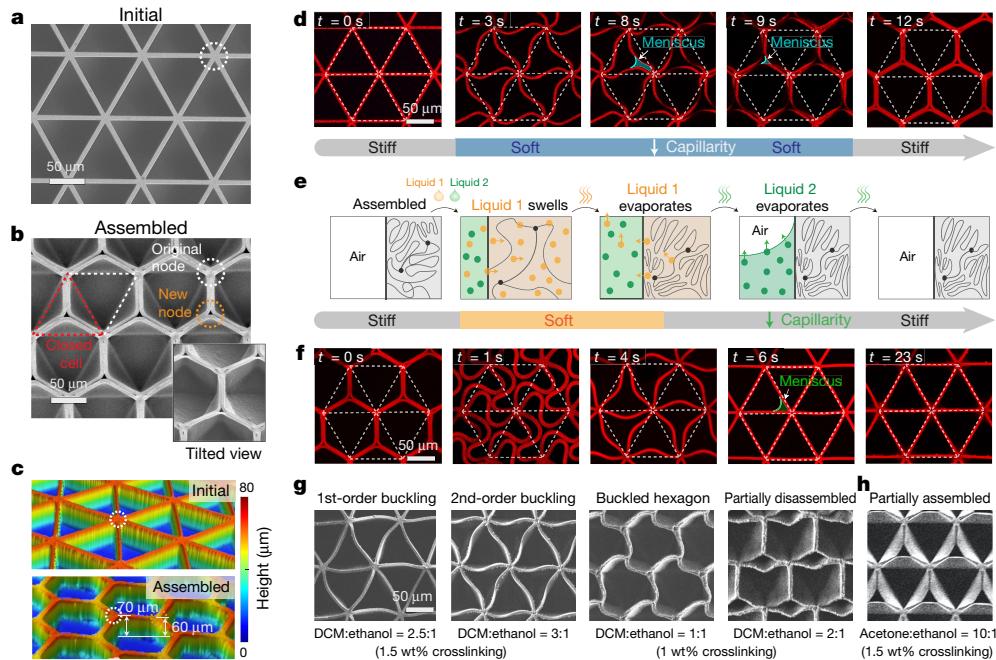
material (Fig. 1b). Critically, as the liquid begins to evaporate from inside the compartments, capillary forces are exerted on the softened structure, acting locally at each individual node and zipping the edges together in a coordinated manner. This leads to a change in the connectivity of the original nodes, or to their disappearance and the creation of new nodes, while also changing the number and coordination of compartments, resulting in transformation to a new lattice topology. Finally, as the liquid rapidly evaporates from inside the material at the molecular scale, the dried structure regains its stiffness and the new geometry remains trapped (Fig. 1b).

To quantitatively investigate such a topological transformation process and to determine the critical elasticity threshold required for full transformation to a new topology, a simplified mathematical model is developed. We focus on two adjacent walls forming an angle α as part of a general cellular structure with edge length l, thickness b and height h. After transformation by capillary, only the upper portion with height h^* is assembled because the bottom of the structure is always attached to the base (Fig. 1c). This upper portion deformation results in stretching ($\propto b$) and folding ($\propto b^2$) of the walls, and dominates the total elastic energy relative to the bending deformation ($\propto b^3$) of the lower part; this assumption holds as long as the height of the structure h is not too small compared to the edge length l. On the other hand, the work done by capillarity is approximated by the capillary forces (γh^*) multiplied by the distance travelled by the menisci (($l/2$)sec($\alpha/2$)) (refs. [27,37,38]), where γ is the surface tension of the liquid. For the capillary assembly to happen, the capillary work must overcome the elastic energy; this simplified energy argument gives a critical Young's modulus for the underlying material (Supplementary Information section 2, Supplementary Fig. 1):

$$E_{cr} = \frac{6\gamma l \sec(\alpha/2)}{3lb[\sec(\alpha/2) - 1 - \delta]^2 + \alpha b^2 (1+\delta)^2}, \quad (1)$$

where δ is the swelling ratio of the material by the liquid. E_{cr} provides an upper limit for the material stiffness above which the transformation will not occur. In Fig. 1d, we present the evolution of E_{cr} as a function of angle α and wall thickness b (varying from 5 μm to 500 μm) for structures with a constant slenderness ratio of $l/b = 15$ and $\gamma = 25 \times 10^{-3}\,N\,m^{-1}$ (for typical volatile liquids, such as acetone). According to the contour plot, E_{cr} decreases drastically down to a few kilopascals with increasing b, indicating that the smallest dimensions (that is, the wall thickness b) of the considered structure must stay within the micrometre scale for reasonable material stiffness. Moreover, E_{cr} also decreases with increasing angle α, showing that structures with larger angles, such as square and hexagonal lattices, are much more difficult to transform than those with smaller angles.

Although our model can predict the assembly behaviour of a wide range of cellular architectures (Supplementary Fig. 2), we selected a triangular ($\alpha = 60°$) micro-cellular structure with dimensions $l = 100\,\mu m$, $b = 7\,\mu m$ and $h = 70\,\mu m$ as an initial experimental test case. For such a structure, equation (1) provides a critical modulus of $E_{cr} \approx 175\,kPa$, which is much lower than that of most commonly used polymers, such as polydimethylsiloxane (PDMS), rubber, polyethylene or epoxy (Fig. 1e). Although there exist soft materials with Young's modulus below E_{cr} (such as Ecoflex or PDMS with low crosslinking density[29], bottle-brush PDMS[28] and hydrogels[39]), they are too sticky or fragile to be compatible with the moulding fabrication procedure of high-aspect-ratio microstructures, and typically undergo permanent distortion after demoulding or irreversible collapse (Supplementary Fig. 3). By contrast, the transient solvent-induced softening allows topological transformation to be extended to polymers with high Young's modulus that can be easily moulded, temporarily plasticized during assembly and restiffened after evaporation. Key features in selecting a polymer–solvent pair suitable for topological transformation are the solubility, volatility and Flory–Huggins parameters[31–33,35], which describe the ability of the

Fig. 2 | Experimental characterization of the assembly and disassembly of a triangular lattice. a, Top view of the initial triangular micro-cellular structure, imaged by a scanning electron microscope. **b**, Top and tilted views of the assembled micro-cellular structure. The initial triangular lattice is transformed to a hexagonal lattice upon application of an acetone droplet (~50 μl for a ~1 cm² sample). One of the new nodes is marked with an orange circle and an original node with a white circle. **c**, Profilometer 3D surface topography of the initial (top) and assembled (bottom) microstructure. Whereas the top surface of the original structure is planar, the assembled structure contains nodes of two different heights owing to the wall deformation. **d**, Fluorescence confocal images of the microstructures at different stages of the assembly. Rhodamine B was co-polymerized into the polymer for characterization by fluorescence confocal microscopy (Supplementary Information section 1.2). **e**, Schematic representation of the generalized mechanism of the disassembly process,
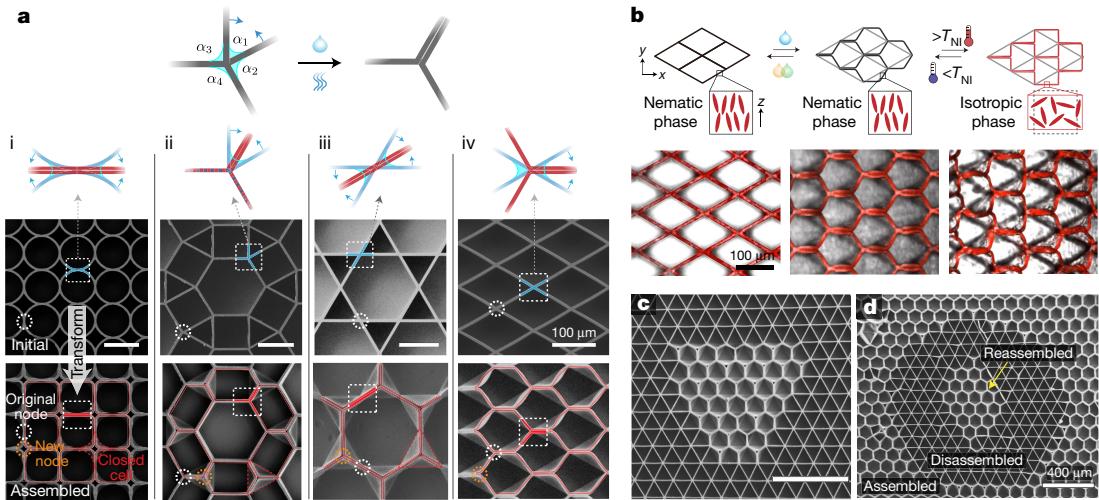
showing how the mixture of two liquids decouples the two scales, with one—highly volatile—liquid acting at the molecular scale and another—chemically inert, less volatile—liquid returning the structure to its original state at the micrometre scale. **f**, Fluorescence confocal images of the LCP microstructures at different stages during the disassembly induced by the DCM:ethanol mixture at 2:1 ratio, with DCM swelling the assembled structure considerably to disassociate the assembled walls, and ethanol exerting capillary forces on a stiffened structure after evaporation of DCM. **g**, Selective trapping of intermediate stages (imaged by a scanning electron microscope) by tuning the evaporation kinetics using different solvent concentrations and polymer compositions. All the presented structures are transformed from the assembled hexagonal lattice (as shown in Fig. 2b). **h**, Partial topological transformation of the initial triangular lattice into a hierarchical triangular lattice with two compartment sizes using a mixture of acetone and ethanol.

solvent to swell and soften the elastic network below E_{cr}, whereas high volatility allows fast transformation. In addition, the properties of the polymer matrix, including the chemical nature, crosslinking density, crystallization (molecular packing/physical crosslinking), porosity, and chain topology[34,36], can be leveraged to modify the solvent–polymer interaction.

As a representative material, a polydomain liquid-crystalline polymer (LCP) with an initial modulus of about 23,000 kPa in the dry state (far above E_{cr}) was selected as a model system (Fig. 1e, Supplementary Fig. 4a). To focus on the material properties of the LCP during the liquid treatment while eliminating complex assembly behaviour, an isolated base-attached LCP microplate was fabricated with the same dimensions as an edge of the considered lattice structure to ensure comparable dynamics and kinetics of evaporation (Fig. 1f). When the plate is swelled by the wetting liquid acetone—a good solvent of the LCP, with a vapour pressure of 30.7 kPa at 25 °C—the solvent molecules penetrate into the polymer matrix, break the packing of the polymer chains and plasticize the material[35,40], reducing the glass transition temperature (T_g) from 58 °C to −30 °C and softening the material drastically down to about 80 kPa (Supplementary Fig. 5), while also swelling the plate to a 10% strain along the top edge. Upon evaporation, T_g returns to 58 °C as the material returns to its original stiffness of about 23,000 kPa, and the dried plate is kinetically trapped with a 9% strain in the glassy state at room temperature; the extended conformation of polymer chains in the swollen state is locked owing to the fast evaporation of liquid in the microscopic system[41,42]. The plate can relax back to its initial length

when heated above T_g as the polymer chains return to the original conformation (Fig. 1f, Supplementary Video 1). According to our theoretical model, such swelling of the material facilitates assembly because it compensates for the required stretching of the walls, and trapping plays a critical role in maintaining the assembly after the capillary force ceases (Fig. 1g). Trapping is expected to occur for materials that have a dry-state T_g that is higher than the ambient temperature. Without this effect, an approximate adhesion energy of 3.3 J m⁻² would be required to hold the restiffened structure together (Supplementary Information section 2.3), which is much higher than the adhesion energy of typically used materials[43,44].

To test our strategy, the triangular cellular microstructure was moulded from LCP by soft lithography (Fig. 2a). Droplets of acetone were placed on horizontal substrates to immerse the cellular structure and allowed to evaporate under ambient conditions (for a systematic study of other liquids, see Supplementary Fig. 6). After evaporation, the upper portion of the triangular lattice was transformed to hexagonal, with triangular geometry retained at the base (Fig. 2b). The transformation results in the change of the fundamental topology of the microstructure: the node connectivity changes from six to three, the number of compartments is halved, and the number of nodes and size of compartments are doubled. Additionally, according to optical three-dimensional (3D) surface profilometry (Fig. 2c, Supplementary Fig. 7), the initial two-dimensional (2D) lattice becomes a true 3D structure with a non-planar top surface after the assembly, owing to the formation of enclosures and a more complex height profile, given

Fig. 3 | Generalization of topological transformation principle. a, The generalized lattice consists of nodes with different angles. The edges forming the smallest angle will undergo zipping for angle-guided capillary-driven transformations from: circular to square (i), rhombitrihexagonal to hybrid hexagonal (ii), kagome to hexagonal (iii) and rhombic to hexagonal (iv). We note that, compared to the triangular-transformed and kagome-transformed hexagonal lattices, which are comprised of nodes connecting three equal double walls, nodes in the hexagonal lattice assembled from the diamond structure comprise two single walls and one double wall, resulting in additional anisotropy along the horizontal direction. **b**, Multi-stimuli deformation of molecularly aligned LCP diamond-shaped cellular structures with the director oriented along the z axis. **c**, **d**, Regional triangular–hexagonal transformations through localized multi-step assembly/disassembly.

that the new nodes formed by the inward-bending plates are 10 μm shorter than the original nodes.
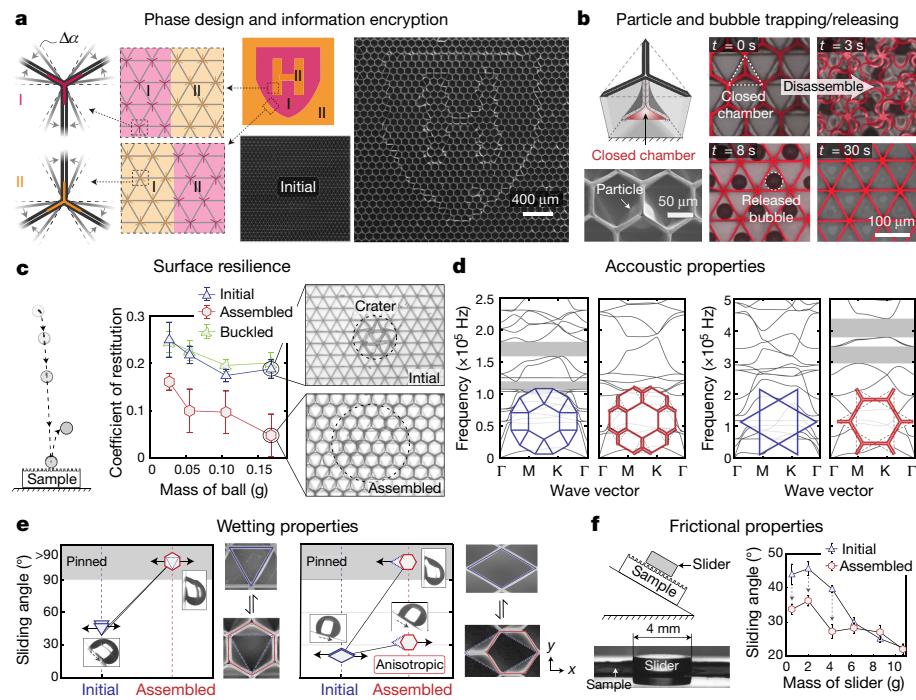
The dynamics of the assembly process was monitored by fluorescent confocal microscopy (Fig. 2d, Supplementary Video 2). Acetone first swells the material, leading to a buckled configuration (at time $t = 3$ s), and upon evaporation forms menisci, where the localized capillary forces break the symmetry of each node ($t = 8$ s). The menisci further zip up the buckled walls and ultimately transform the node connectivity from six to three ($t = 9$ s) with neighbouring nodes transforming coordinately, forming ordered domains (Supplementary Fig. 8). Finally, as the material de-swells, the structure is locked in the hexagonal topology with straightened double walls ($t = 12$ s). Both trapping of the material and adhesion between the assembled walls contribute to retaining the new topology, which remains robust under harsh conditions, including heating above T_g or immersing in various non-swelling liquids for several days (Supplementary Fig. 9, Supplementary Video 3).

Disassembling the structure and restoring the original topology requires overcoming both the kinetic trapping of the polymer conformation and the interfacial adhesion between the walls. Although heat or plasticizers can untrap the material, they also tend to decrease the elastic restoring force. Both requirements can be fulfilled simultaneously by applying a liquid that swells the underlying material with a much greater swelling ratio than that of the liquid used for the assembly, to trigger drastic bending of the assembled walls that overcomes the adhesion and leads to the dissociation of the walls, initiating disassembly. However, as the liquid evaporates, the formed menisci would tend to reassemble the structure. To reduce the capillary forces, a second liquid—less volatile, but non-swelling—is mixed with the first one to delay any capillary forces until after the material has finished disassembling and has become stiff again (Fig. 2e). To demonstrate this unique disassembly mechanism experimentally, we used a mixture of dichloromethane (DCM)—a good solvent of LCP, that swells the LCP substantially (with >30% strain)—as the first volatile liquid (vapour pressure of 57.3 kPa at 25 °C) and ethanol—a poor solvent of the LCP—as the second, less volatile liquid (vapour pressure of 5.95 kPa at 25 °C) (Fig. 2f, Supplementary Video 4). Compared to the assembly process in which a single liquid both softens the material at the molecular scale and generates capillary forces at

the architectural scale, the mixture enables modular control over the timescales of the two actions, with DCM controlling the molecular scale and ethanol governing the architectural scale separately and consecutively to yield desired outcomes.

In addition to restoring the original triangular structure, such modular control enables trapping of a series of intermediate states during disassembly by varying the DCM–ethanol ratio, which affects both the swelling extent of the LCP and the volatility of DCM when dispersed in ethanol, and thus the trapping strain and modes of disassembly (Fig. 2g). Similar concepts can also be used to tailor the original assembly process. For example, Fig. 2h shows that partial assembly of the triangular lattice can be achieved by adding to acetone a trace amount of ethanol, which diminishes the softening effect and increases the elastic restoring energy during assembly. Notably, the assembly and disassembly processes take only seconds and are highly reversible and fatigue-free (Supplementary Fig. 10), enabling a durable and fast switching between different topologies of microstructures.

The methodology can be generalized to different geometries with more complex symmetries, anisotropies, and combinations of compartment shapes and sizes. An arbitrary lattice can be considered as a combination of nodes connected to edges that form different angles, with the capillary forces preferentially assembling edge pairs with smaller angles (Fig. 3a). On the basis of this principle, we designed and experimentally tested a variety of cellular architectures undergoing programmed, robust topological transitions (Fig. 3a, Supplementary Fig. 11). The approach is also readily applicable to structures with different dimensions and to other polymeric materials (Supplementary Figs. 12, 13). It can also be integrated with orthogonal response mechanisms to enable multimodal transformations of a given lattice upon application of different triggers. For example, LCPs can be imprinted with anisotropic thermal responses by aligning the liquid-crystal molecules inside the cellular structures into a nematic liquid-crystalline phase (Supplementary Fig. 13b)[45,46]. Figure 3b presents an exemplary diamond lattice with the liquid-crystal director aligned perpendicular to the base[47] that is transformed to a hexagonal lattice via capillary assembly, and then to a brick pattern by heating to above its thermal nematic-to-isotropic phase-transition temperature (>T_{NI}) (Supplementary Video 5). We further note that the presented strategy is applicable to any 2D or 3D

Fig. 4 | Exemplary applications of lattice structures undergoing topological transformations. a, Information encryption. Harvard shield outlined by the engineered phase boundaries appears upon topological transformation of the triangular lattice. **b**, Particle and bubble trapping/releasing through the closed chambers formed by topological transformation. **c**, Ball bouncing test carried out to measure the resilience of the surface before and after transformation. Error bars represent the standard deviation of eight geometries, including base-attached or free-standing ones (see Supplementary Fig. 14). Here we intentionally choose a rigid-base-attached configuration for its better structural stability, applicability to any lattice geometry, and the ability to form closed cavities upon topological transformation—a unique compartmentalization feature explored in applications described below. Moreover, we demonstrate interesting region-specific assembly–disassembly transformations through the application of small droplets locally—another property unachievable with global fields (Fig. 3c, d, Supplementary Fig. 15).

measurements. We note that the topological transformation is necessary to change the coefficient of restitution, as simply buckled (presented in Fig. 2g) and undeformed structures show the same resilience. **d**, Bandgaps can be tuned by capillarity-driven assembly for some lattices. Examples for bandgaps in rhombitrihexagonal and kagome lattices are shown. **e**, **f**, Controlling surface properties upon topological transformations: wetting (**e**); friction (**f**). Error bars represent the standard deviation of three measurements.

By carefully programming the spatial distribution of angular perturbations at each node, we can eliminate or engineer the location of domain boundaries in assembled structures (Supplementary Information section 3.8, Supplementary Figs. 16, 17, Supplementary Video 6). Considering the large triangular lattice shown in Fig. 4a, the nodes inside the magenta region are designed to transition to Y-shaped (phase I), and the nodes inside the orange region are programmed to transition to inverted Y-shaped (phase II). The written-in phase information is not optically visible before assembly, and becomes evident only after solvent treatment (Fig. 4a, Supplementary Fig. 17). The information encryption and read-out can be reversed by treating the LCP microstructure with different solvent systems as discussed previously. We note that the location information of the designed phase boundaries is not merely stored on the phase boundaries, but encoded in every node of the structure via their preferred phase, which makes such information encryption extremely robust.

Topological changes of the cellular surfaces—such as the closure of subsets of compartments and the ability to induce global or localized transformations—provide opportunities for a number of applications. As shown in Fig. 4b, the cellular surface can selectively trap and sort microparticles with diameters <50 μm that are able to enter the initially triangular compartment. Furthermore, the closed chambers also create ordered cavities that each capture and release uniform microscale bubbles upon assembly–disassembly (Fig. 4c, Supplementary Video 7) that can be used as miniaturized chemical reaction chambers. The resilience of the cellular surface also changes considerably after the topological transformation, as demonstrated by the ball-bouncing test results (Fig. 4d, Supplementary Video 7). Compared to the uniform or buckled triangular structure that displays broken walls upon impact, the transformed hexagonal surface exhibits larger craters with no detectable structural damage. We believe that the formed closed chambers constitute a cushion layer and offer extra structural flexibility, which increases the efficiency in absorbing the impact energy.

The change of geometry, combined with the formation of double walls, also serves as a platform for tunable phononic crystals, in which the bandgaps and propagation velocity of elastic waves can be altered reversibly (Fig. 4e). As noted above, the 3D height profile of the structure is also changed through edge assembly and node formation (Fig. 2c), giving rise to modified surface planarity and anisotropy that affect surface properties such as wetting and friction (Fig. 4f), and both surface properties can be further changed by localized, areal topological transformations. For example, the surface becomes much more adhesive to water droplets when transformed from a triangular to a non-planar hexagonal lattice (Supplementary Video 7), which can most probably be attributed to the pinning points that are created when new nodes form and to the overall elongation of walls that causes the water–polymer contact area to increase slightly. Moreover, anisotropic, directional wetting properties can be achieved through a diamond-to-hexagon transformation in which the initial diamond lattice shows an isotropic wetting along the *x* axis, but after assembly the sliding angle towards the left is much higher (>90°, pinned) than towards the right (~34°). This can be explained by the asymmetric tetrahedral containers formed by the slanted walls that pin the left-travelling droplet to the surface. Similarly, the friction coefficient of the cellular surface is also tunable via topological transformations (Fig. 4g).

In conclusion, we have presented a simple, widely applicable strategy that gives rise to complex topological transformations of cellular microstructures. The defining feature of our approach is that the applied liquid has a dual role by acting at two scales: it transiently softens and swells the material at the molecular level and creates an intricate network of localized capillary forces at the architectural scale, and these actions at two scales take place in a sequentially controlled manner. Modular control over the timing and extent of the softening/ restiffening/evaporation events through customized polymer–liquid pairs enables reversibility and switching between various intermediate topologies. Our theoretical model provides a quantitative foundation for rationally guiding the materials selection and structural design. Compared to existing reconfiguration methods—which produce buckling or shearing deformations without controllable topological changes[16–23]; are often either irreversible or unable to hold the reconfigured shape without external stimuli[16,18,19]; or require complex material compositions, sophisticated and costly fabrication procedures that are not applicable at the microscale[17,19,20], and/or long response times[18,20]— our strategy enables extremely fast, robust and reversible topological transformations and is compatible with a simple moulding fabrication procedure. The demonstrated applications can be integrated with global or localized transformations, phase boundary design and active materials responding to orthogonal stimuli, to control functional properties across different scales and application fields. In principle, our strategy can be applied to nanoscale structures and will open avenues for designing tunable photonic meta-surfaces in which the topology has a key role. The opportunities offered by this strategy to systematically manipulate the topological transformation provide a platform for the fundamental study of the topology–dimension–material relation and the underlying multiscale physicochemical mechanisms.

Online content

Any methods, additional references, Nature Research reporting summaries, source data, extended data, supplementary information, acknowledgements, peer review information; details of author contributions and competing interests; and statements of data and code availability are available at https://doi.org/10.1038/s41586-021-03404-7.

1. Gibson, L., Ashby, M. & Harley, B. *Cellular Materials in Nature and Medicine* (Cambridge Univ. Press, 2010).
2. Gibson, L. J. & Ashby, M. F. *Cellular Solids: Structure, Properties and Applications* (Cambridge Univ. Press, 1999).
3. Ruzzene, M., Scarpa, F. & Soranna, F. Wave beaming effects in two-dimensional cellular structures. *Smart Mater. Struct.* **12**, 363–372 (2003).
4. He, H. et al. Topological negative refraction of surface acoustic waves in a Weyl phononic crystal. *Nature* **560**, 61–64 (2018).
5. Kang, S. et al. Stretchable lithium-ion battery based on re-entrant micro-honeycomb electrodes and cross-linked gel electrolyte. *ACS Nano* **14**, 3660–3668 (2020).
6. Shirman, E. et al. Modular design of advanced catalytic materials using hybrid organic– inorganic raspberry particles. *Adv. Funct. Mater.* **28**, 1704559 (2018).
7. Kim, O. H. et al. Ordered macroporous platinum electrode and enhanced mass transfer in fuel cells using inverse opal structure. *Nat. Commun.* **4**, 2473 (2013).
8. Muth, J. T., Dixon, P. G., Woish, L., Gibson, L. J. & Lewis, J. A. Architected cellular ceramics with tailored stiffness via direct foam writing. *Proc. Natl Acad. Sci. USA* **114**, 1832–1837 (2017).
9. Christensen, R. M. Mechanics of low density materials. *J. Mech. Phys. Solids* **34**, 563–578 (1986).
10. Coulais, C., Sabbadini, A., Vink, F. & van Hecke, M. Multi-step self-guided pathways for shape-changing metamaterials. *Nature* **561**, 512–515 (2018).
11. Gan, Z., Turner, M. D. & Gu, M. Biomimetic gyroid nanostructures exceeding their natural origins. *Sci. Adv.* **2**, e1600084 (2016).
12. Maloney, K. J. et al. Multifunctional heat exchangers derived from three-dimensional micro-lattice structures. *Int. J. Heat Mass Transf.* **55**, 2486–2493 (2012).
13. Khan, M. I. H., Farrell, T., Nagy, S. A. & Karim, M. A. Fundamental understanding of cellular water transport process in bio-food material during drying. *Sci. Rep.* **8**, 15191 (2018).
14. Zhang, R., Hao, P., Zhang, X. & He, F. Dynamics of high Weber number drops impacting on hydrophobic surfaces with closed micro-cells. *Soft Matter* **12**, 5808–5817 (2016).
15. Kim, J. J., Bong, K. W., Reátegui, E., Irimia, D. & Doyle, P. S. Porous microwells for geometry-selective, large-scale microparticle arrays. *Nat. Mater.* **16**, 139–146 (2017).
16. Kang, S. H., Shan, S., Noorduin, W. L., Khan, M., Aizenberg, J. & Bertoldi, K. Buckling-induced reversible symmetry breaking and amplification of chirality using supported cellular structures. *Adv. Mater.* **25**, 3380–3385 (2013).
17. Boley, J. W. et al. Shape-shifting structured lattices via multimaterial 4D printing. *Proc. Natl Acad. Sci. USA* **116**, 20856–20862 (2019).
18. Zhang, H., Guo, X., Wu, J., Fang, D. & Zhang, Y. Soft mechanical metamaterials with unusual swelling behavior and tunable stress-strain curves. *Sci. Adv.* **4**, eaar8535 (2018).
19. Kim, Y., Yuk, H., Zhao, R., Chester, S. A. & Zhao, X. Printing ferromagnetic domains for untethered fast-transforming soft materials. *Nature* **558**, 274–279 (2018).
20. Xia, X. et al. Electrochemically reconfigurable architected materials. *Nature* **573**, 205–213 (2019).
21. Coulais, C., Teomy, E., De Reus, K., Shokef, Y. & van Hecke, M. Combinatorial design of textured mechanical metamaterials. *Nature* **535**, 529–532 (2016).
22. Haghpanah, B., Salari-Sharif, L., Pourrajab, P., Hopkins, J. & Valdevit, L. Multistable shape-reconfigurable architected materials. *Adv. Mater.* **28**, 7915–7920 (2016).
23. Fu, H. et al. Morphable 3D mesostructures and microelectronic devices by multistable buckling mechanics. *Nat. Mater.* **17**, 268–276 (2018).
24. Bico, J., Roman, B., Moulin, L. & Boudaoud, A. Elastocapillary coalescence in wet hair. *Nature* **432**, 690 (2004).
25. Pokroy, B., Kang, S. H., Mahadevan, L. & Aizenberg, J. Self-organization of a mesoscale bristle into ordered, hierarchical helical assemblies. *Science* **323**, 237–240 (2009).
26. Kang, S. H., Pokroy, B., Mahadevan, L. & Aizenberg, J. Control of shape and size of nanopillar assembly by adhesion-mediated elastocapillary interaction. *ACS Nano* **4**, 6323–6331 (2010).
27. Roman, B. & Bico, J. Elasto-capillarity: deforming an elastic structure with a liquid droplet. *J. Phys. Condens. Matter* **22**, 493101 (2010).
28. Cai, L. H. et al. Soft poly(dimethylsiloxane) elastomers from architecture-driven entanglement free design. *Adv. Mater.* **27**, 5132–5140 (2015).
29. Jeong, S. H., Zhang, S., Hjort, K., Hilborn, J. & Wu, Z. PDMS-based elastomer tuned soft, stretchable, and sticky for epidermal electronics. *Adv. Mater.* **28**, 5830–5836 (2016).
30. Matsunaga, M., Aizenberg, M. & Aizenberg, J. Controlling the stability and reversibility of micropillar assembly by surface chemistry. *J. Am. Chem. Soc.* **133**, 5545–5553 (2011).
31. Flory, P. J. *Principles of Polymer Chemistry* (Cornell Univ. Press, 1953).
32. Rubinstein, M. & Colby, R. H. *Polymer Physics* (Oxford Univ. Press, 2003).
33. Dimarzio, E. A. & Gibbs, J. H. Molecular interpretation of glass temperature depression by plasticizers. *J. Polym. Sci. A* **1**, 1417–1428 (1963).
34. Lin, H. et al. Organic molecule-driven polymeric actuators. *Macromol. Rapid Commun.* **40**, 1800896 (2019).
35. Du, H. & Zhang, J. Solvent induced shape recovery of shape memory polymer based on chemically cross-linked poly(vinyl alcohol). *Soft Matter* **6**, 3370–3376 (2010).
36. Gu, Y., Zhao, J. & Johnson, J. A. Polymer networks: from plastics and gels to porous frameworks. *Angew. Chem. Int. Ed.* **59**, 5022–5049 (2020).
37. Holmes, D. P., Brun, P. T., Pandey, A. & Protière, S. Rising beyond elastocapillarity. *Soft Matter* **12**, 4886–4890 (2016).
38. Wei, Z. et al. Elastocapillary coalescence of plates and pillars. *Proc. R. Soc. A Math. Phys. Eng. Sci.* **471**, 20140593 (2015).
39. Calvert, P. Hydrogels for soft machines. *Adv. Mater.* **21**, 743–756 (2009).
40. Chow, T. S. Molecular interpretation of the glass transition temperature of polymer-diluent systems. *Macromolecules* **13**, 362–364 (1980).
41. Rath, A., Geethu, P. M., Mathesan, S., Satapathy, D. K. & Ghosh, P. Solvent triggered irreversible shape morphism of biopolymer films. *Soft Matter* **14**, 1672–1680 (2018).
42. Zhu, X., Wu, G., Dong, R., Chen, C. M. & Yang, S. Capillarity induced instability in responsive hydrogel membranes with periodic hole array. *Soft Matter* **8**, 8088–8093 (2012).
43. Myshkin, N. & Kovalev, A. Adhesion and surface forces in polymer tribology—a review. *Friction* **6**, 143–155 (2018).
44. Israelachvili, J. N. *Intermolecular and Surface Forces* (Academic Press, 2011).
45. White, T. J. & Broer, D. J. Programmable and adaptive mechanics with liquid crystal polymer networks and elastomers. *Nat. Mater.* **14**, 1087–1098 (2015).
46. Ohm, C., Brehmer, M. & Zentel, R. Liquid crystalline elastomers as actuators and sensors. *Adv. Mater.* **22**, 3366–3387 (2010).
47. Yao, Y. et al. Multiresponsive polymeric microstructures with encoded predetermined and self-regulated deformability. *Proc. Natl Acad. Sci. USA* **115**, 12950–12955 (2018).

Article

Data availability

The data supporting the findings of this study are included within the paper and its Supplementary Information files and are available from the corresponding author upon reasonable request.

Author contributions S.L., B.D., K.B. and J.A. conceived and initiated the project. S.L., A.S.-Y., J.K., R.S.M. and C.T.Z. performed the experiments. B.D. performed the theoretical modelling and image analysis. J.L. and S.Y. performed the finite-element modelling and pattern designs. S.L., B.D. and A.G. analysed the experimental data. K.B. and J.A. supervised the project. All co-authors provided useful feedback and contributed to the manuscript.

Competing interests The authors declare no competing interests.

Additional information
Supplementary information The online version contains supplementary material available at https://doi.org/10.1038/s41586-021-03404-7.
Correspondence and requests for materials should be addressed to J.A.
Peer review information *Nature* thanks Robin Ras, Arnaud Saint-Jalmes, Scott Waitukaitis and the other, anonymous, reviewer(s) for their contribution to the peer review of this work. Peer reviewer reports are available.
Reprints and permissions information is available at http://www.nature.com/reprints.